Human TMEM16K (ANO10)

A Target Enabling Package (TEP)

Gene ID / UniProt ID / EC	**55129** / Q9NW15
Target Nominator	Paolo Tammaro (Oxford), Alessio Accardi (Cornell), Andrea Nemeth (Oxford)
SGC Authors	Simon R. Bushell, Ashley C.W. Pike, Chitra A. Shintre, Annamaria Tessitore, Amy Chu, Qinrui Wang, Leela Shrestha, Shubhashish Mukhopadhyay, Nicola A.Burgess-Brown, Liz Carpenter.
Collaborating Authors	Maria E. Falzone[1], Nils J.G. Rorsman[2], Chau M. Ta[2], Robin A. Corey[3], Thomas D. Newport[3], John C. Christianson[4], Lara F. Scofara[2], James D. Love[5], Rebecca Sitsapesan[2], Phillip J. Stansfeld[3], Juha T. Huiskonen[6], Paolo Tammaro[2], Alessio Accardi[1,7,8].
Target PI	Liz Carpenter
Therapeutic Area(s)	Neurological diseases
Disease Relevance	Mutation to ANO10 causes autosomal recessive spinocerebellar ataxia type 10 (SCAR10)
Date Approved by TEP Evaluation Group	June 10, 2019
Document version	Version 1
Document version date	June 2019
Citation	Simon R. Bushell, Ashley C. W. Pike, Maria E. Falzone, Nils J. G. Rorsman, Chau M. Ta, Robin A. Corey, … Elisabeth P. Carpenter. (2019). Human TMEM16K (ANO10); A Target Enabling Package [Data set]. Zenodo. 10.5281/zenodo.3245350
Affiliations	1. Department of Biochemistry, Weill Cornell Medical School. 2. Department of Pharmacology, University of Oxford. 3. Department of Biochemistry, University of Oxford. 4. Nuffield Department of Rheumatology, Orthopaedics and Musculoskeletal Sciences, University of Oxford. 5. Albert Einstein College of Medicine, Department Of Biochemistry. 6. Oxford Particle Imaging Centre, Division of Structural Biology, Wellcome Trust Centre for Human Genetics, University of Oxford. 7. Department of Anesthesiology, Weill Cornell Medical School. 8. Department of Physiology and Biophysics, Weill Cornell Medical School.

USEFUL LINKS

(Please note that the inclusion of links to external sites should not be taken as an endorsement of that site by the SGC in any way)

SUMMARY OF PROJECT

There are ten members of the TMEM16/Anoctamin family of proteins in mammals. Although the first members of this family to be discovered, TMEM16A and TMEM16B, have a calcium-regulated chloride channel function, subsequently other members of the family, such as TMEM16F, were found to have lipid scramblase activity combined with non-selective ion channel activity. TMEM16K was a relatively understudied member of the family despite the observation that mutations in TMEM16K have been linked to the genetic disease autosomal recessive spinocerebellar ataxia Type 10 (Also known as SCAR10 or ARCA3). SCAR10 is a late-onset neurodegenerative disorder which causes marked atrophy of the cerebellum with consequential deterioration in limb co-ordination, speech and eye movement. We have solved several structures of human TMEM16K through X-ray crystallography and cryo-EM capturing both active and inactive conformational states. Through collaborations, we have investigated TMEM16K's function and location in cells. We were able to show that TMEM16K acts as a lipid scramblase with non-selective ion channel activity that is sensitive to both Ca^{2+} and lipid chain lengths. We also showed that TMEM16K mainly

resides in the endoplasmic reticulum where it may be regulated by the ER's unique lipid profile. Our highest resolution cryo-EM structure for TMEM16K allowed us to identify a bound lipid in the cavity behind the groove that transports the lipid headgroups and this lipid binding site may represent an allosteric modulator site, providing a direction for the design of binders which could modulate TMEM16K activity in cells.

SCIENTIFIC BACKGROUND

Lipid Scrambling

Lipid bilayers surround cells and organelles and in most membranes, with the exception of the endoplasmic reticulum (ER), the composition of the two leaflets of the bilayer differ. Phospholipid scramblase (PLS) proteins are integral membrane proteins that abolish lipid asymmetry by facilitating the two-way transfer of lipids between membrane envelopes along concentration gradients. Many lipids are synthesised on the cytoplasmic face of the ER and yet the ER has a relatively even distribution of lipids. However, the nature of the phospholipid scramblases in the ER was not clear.

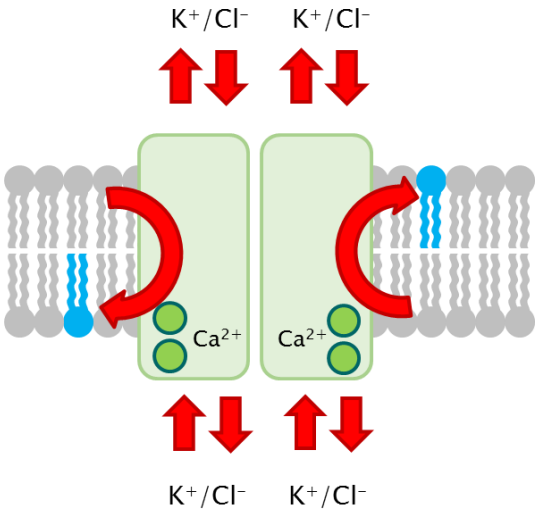

Fig. 1 TMEM16-mediated Lipid Scrambling and non-specific ion channel activity

The TMEM16 family of membrane proteins were originally identified as a class of calcium activated chloride channels called anoctamins, with TMEM16A being the most well studied member of the family (1). Subsequently, many TMEM16 proteins were found to also act as phospholipid scramblases, which are sensitive to the concentration of calcium and have non-specific ion channel activity. Structural investigation of TMEM16 homologues (2) identified a recessed hydrophilic 'groove' formed by several of TMEM16's transmembrane helices as the main facilitator of its PLS activity. These grooves are lined with polar residues, providing a path for lipids to traverse the membrane through transient contacts with hydrophilic lipid headgroups.

TMEM16 Family Disease Linkages

Genetic disruption of TMEM16 PLS activity forms the basis of several inherited disorders. Mutation of TMEM16F causes Scott Syndrome (3), a blood coagulation disorder linked to reduced presentation of phosphatidylserine (PS) on the surface of platelet cells; a key trigger for clot formation. TMEM16E mutation has been linked to disorders of the musculoskeletal system; specifically gnathodiaphyseal dysplasia (4) and limb girdle muscular dystrophy (5,6). TMEM16K (*ANO10*) mutation is linked to autosomal recessive spinocerebellar ataxia, type 10 (also known as SCAR10 or ARCA3) (7-9). SCAR10 patients display progressive atrophy of the cerebellum (**Fig. 2**) with resulting symptoms including cognitive impairment, deterioration of motor skills and epilepsy. Many patients also report a Co-enzyme Q10 deficiency (7).

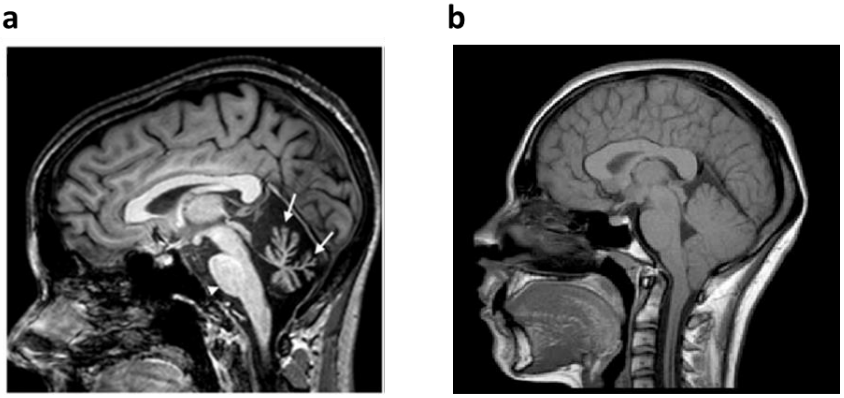

Fig. 2 MRI Images showing cerebellar atrophy in **(a)** SCAR10 Patient and **(b)** healthy individual. Images from *Bodranghien et al (2017)* (10)

TMEM16K

Despite having a wide expression profile, little is known about TMEM16K's cellular role. Previous studies have hinted at TMEM16K being localised intracellularly (11) hampering investigation into any potential PLS or ion flux activity which traditionally rely on plasma membrane expression to easily characterise using conventional techniques. Mutagenesis studies in cells have suggested a role in the regulation of calcium signalling (12), though whether this a direct or indirect consequence of TMEM16K dysfunction remains unclear.

RESULTS – THE TEP

Proteins

We have generated constructs for full-length human TMEM16K with a TEV-cleavable C-terminal 10xHistidine-FLAG tag. The constructs were used to make viruses to express protein in transduced insect (Sf9) and mammalian (Expi293) cells. Overexpressed protein was solubilised from lysed cell membranes using 1% n-undecyl-β-D-maltopyranoside (UDM), supplemented with cholesteryl hemisuccinate (CHS) (10:1 detergent/CHS). After solubilisation, protein was purified in the presence of 0.044% UDM (w/v), 0.0044% CHS (w/v), 20 mM HEPES, pH 7.5, 200 mM NaCl, 5% (w/v) glycerol. Purification was performed using immobilised metal affinity chromatography on TALON® resin, followed by overnight cleavage using Tobacco Edge Virus (TEV) protease to remove the purification tags. Uncleaved protein, co-purified contaminants and TEV protease were removed by reverse IMAC purification. The cleaved protein was then further purified using size exclusion chromatography on a Superose 6 column. Peak fractions were concentrated to approximately 25mg/ml for crystallisation experiments. Final yields of TMEM16K equated to approximately 0.15 mg per L Sf9 culture. Yields were generally higher when TMEM16K was expressed in Expi293 cells.

Structures

Our work has produced 5 structures using both X-ray crystallography and cryogenic electron microscopy (Cryo-EM) techniques.

X-ray Crystallography

- 3.2 Å structure from crystals grown by lipidic cubic phase (LCP) crystallisation (PDB: 5OC9)
- 3.5 Å structure from crystals grown using vapour diffusion (VD) crystallisation (PDB: 6R65)

Cryo-EM

- 3.5 Å structure of TMEM16K in the presence of 2 mM Ca^{2+} ("high Ca^{2+}") (PDB: 6R7X, EMDB: EMD-4746)
- 4.2 Å structure of TMEM16K in the presence of 430 nM ("low Ca^{2+}") (PDB: 6R7Y, EMDB: EMD-4747)
- 5.1 Å Ca^{2+} free TMEM16K structure (10 mM EGTA), (PDB: 6R7Z, EMDB: EMDB-4748)

All structures show the typical TMEM16 bi-lobal "butterfly" dimer fold. This consists of an N-terminal ferrodoxin-like cytoplasmic domain, followed by a transmembrane domain with ten membrane-spanning helices (**Fig. 3**). In addition to the previously identified two calcium binding site located proximal to the scramblase groove, our structures reveal a previously uncharacterised calcium binding site located near the dimer interface. Mutation of Asp615, a key component of this novel binding site, has previously been linked to SCAR10 (7), although the effect this mutation has on protein function and biogenesis remains unclear.

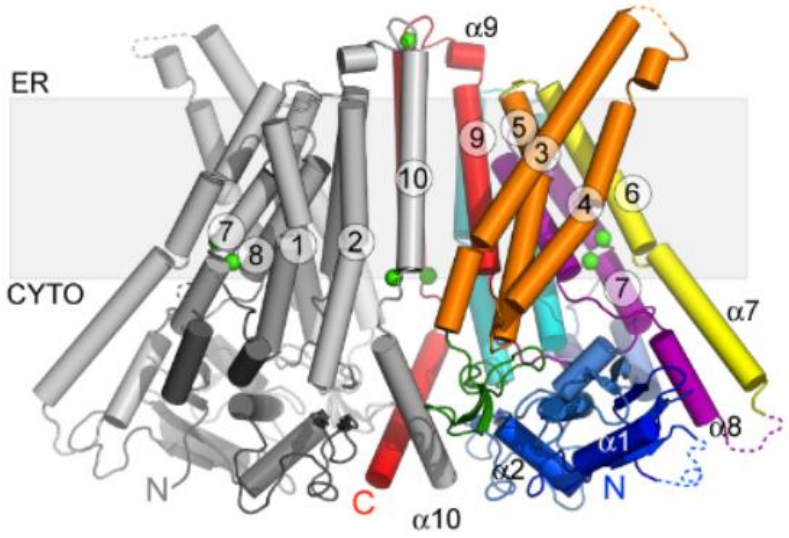

Fig. 3 LCP Crystal Structure of TMEM16K (PDB:5OC9)

A key finding from our structural investigations concerns TMEM16K's switching between active and inactive conformations. Our cryo-EM structures, obtained in more physiologically relevant concentrations of calcium, show TMEM16K in a closed state, with TM3 and TM4 moving across to occlude the transmembrane scrambling groove, compared to the open conformation seen in our crystal structures (**Fig. 3A**). The trigger for TM3-4 movement appears to be rearrangements at the dimer interface, manifesting in the movement of a C-terminal domain-swapped alpha helix, α10, against the β9-β10 hairpin at the cytoplasmic end of TM3-4 (**Fig. 4A**). This pushes and rotates TM3-5, closing the groove (**Fig. 4B-C**).

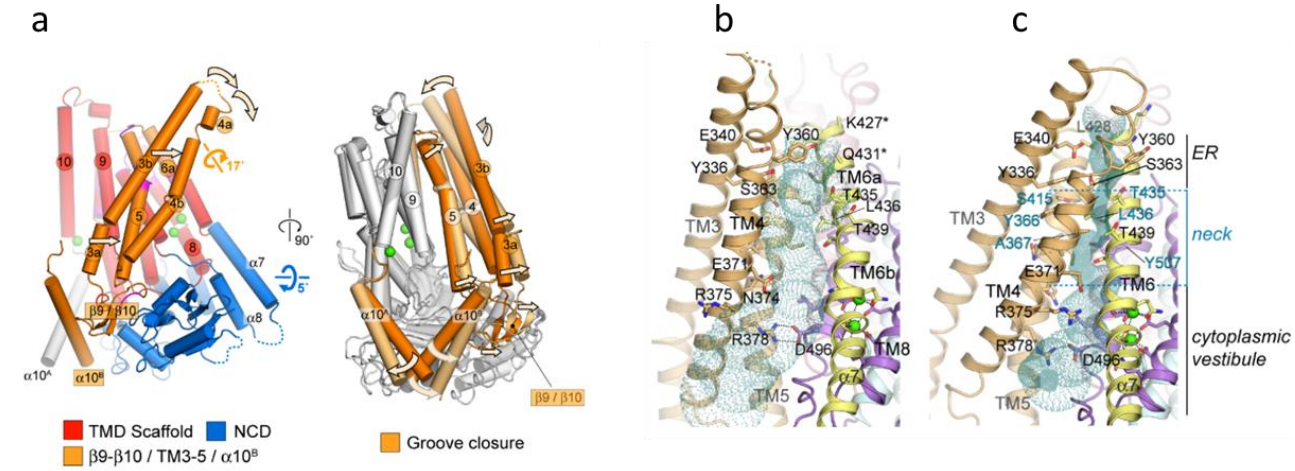

Fig. 4 Active and Inactive Conformations of TMEM16K (**A**) Relative movement of N-terminal cytoplasmic domain (blue, "NCD"), and scramblase groove elements (orange) around the fixed "scaffold" domain (red) **(B-C)** Ribbon representation and key residues of the TMEM16K scrambling groove in open (**B**) and **c**losed (**B**) conformations

These structural changes are not dependent on calcium binding as all binding sites are occupied regardless of conformation in both the X-ray and cryo-EM structures in 2 mM and 430 nM Ca^{2+}. A lower resolution structure of TMEM16K in 10 mM EGTA also showed a closed conformation, with small movements of TM6

adjacent to the Ca^{2+} binding site, but no larger conformational changes. Our functional characterisation of TMEM16K seeks to understand what biological triggers underpin this conformational rearrangement.

Assays

Phospholipid Scramblase (PLS) Assay

The phospholipid scramblase assays are performed by our collaborators Alessio Accardi and Maria Falzone (Cornell, New York, USA). Purified TMEM16K was reconstituted into proteoliposomes made from defined phospholipid mixtures. Proteoliposomes are supplemented with ~0.4% (w/w) fluorescent nitrobenzoxadiazole (NBD) labelled lipids (Ex: 470 nm, Em: 530 nm). NBD fluorescence is extinguished in the presence of dithionite [$(S_2O_4)^{2-}$] ions through the irreversible formation of a covalent adduct. In the absence of PLS activity, NBD-labelled lipids on the inner leaflet of the proteoliposome will be protected from externally added 30 mM sodium dithionite, resulting in a 50 % reduction in overall fluorescence. If a lipid scramblase is present, inner leaflet NBD-lipids will be scrambled, exposing their headgroups on the proteoliposome surface. There they will be quenched by dithionite, resulting in a further drop in fluorescence (**Fig. 5**).

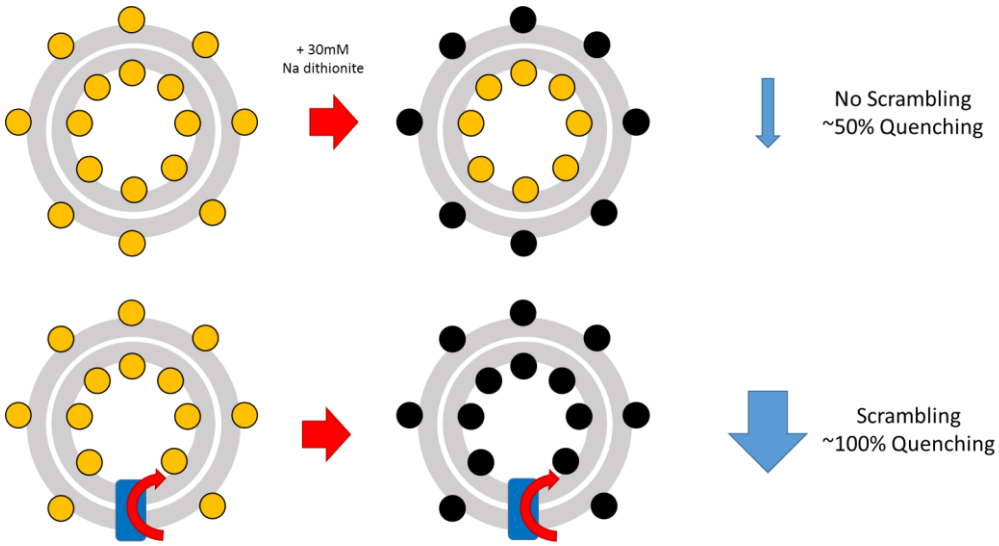

Fig. 5: Assessing Phospholipid Scrambling Activity using NBD-labelled Lipids

Using this assay, we determined that TMEM16K is indeed a calcium-dependent lipid scramblase with rates of lipid scrambling 4-5x higher in the presence of calcium than in its absence (**Fig. 6A**). In addition to its preference for calcium, the rate of TMEM16K-mediated PLS activity was found to be highly dependent on the proteoliposome's lipid composition. When using a 50:50 mixture of short-chain (14:0C) and long chain

(16:0-18:1C) phospholipids, TMEM16K was found to have a scrambling rate 10x higher than when using long chain lipids alone (**Fig. 6A**).

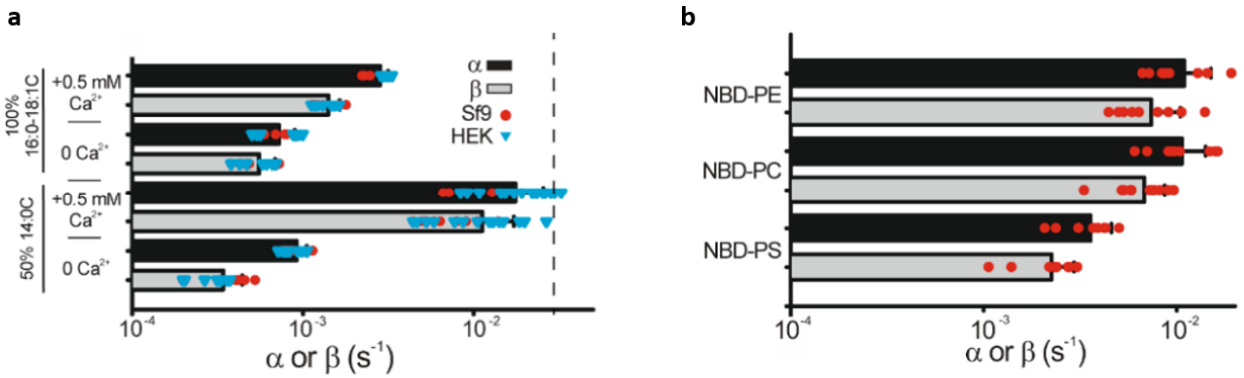

Fig. 6: (A) Comparison of TMEM16K Ca-Dependent PLS Activity in Long-Chain and Mixed Short Chain Lipid Mixtures. Blue Triangles and red circles represent replicates using TMEM16K purified from Expi293F (HEK) and Sf9 Cells respectively. α and β represent rates of inward and outward movement of lipids between bilayer envelopes respectively (B) Rates of scrambling of different NBD-lipid species. Note the lower scrambling rate for NBD-PS.

TMEM16K was also shown to have some preference for the lipids it was able to specifically transfer, with NBD-labelled phosphatidylserine (NBD-PS) scrambling at a slower rate than for similarly labelled phosphatidylcholine (NBD-PC) and phosphatidylethanolamine (NBD-PE) (**Fig. 6B**).

Endpoint Ion Flux Assay

Reconstituted proteoliposomes were also used to measure potential TMEM16K ion channel activity. Proteoliposomes were made in the presence of 300 mM KCl before being transferred to a low Cl^- buffer where they are disrupted by detergent and [Cl^-] measured using a $AgCl_2$ electrode. By comparing the final chloride concentrations in the buffer compared to that of a protein-free liposome control, one can measure endpoint ion channel activity (**Fig. 7A**).

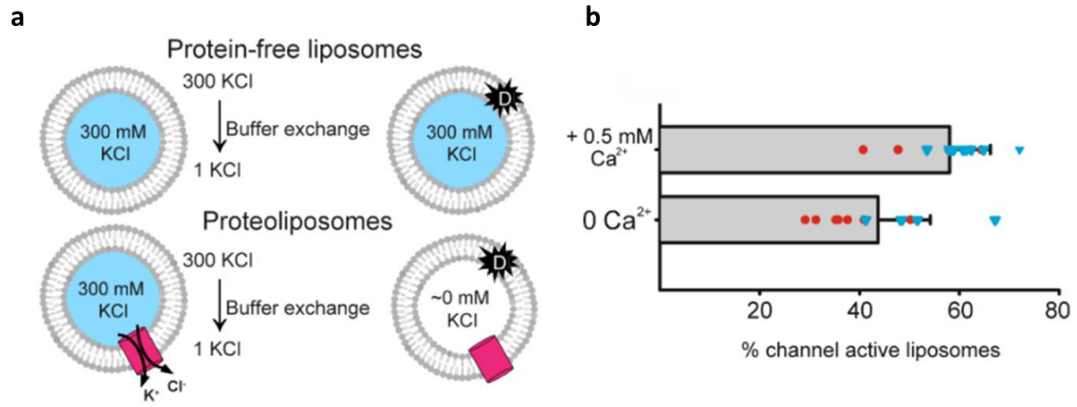

Fig. 7: (A) Schematic demonstrating TMEM16K Ion Flux Assay. (B) Percent channel active TMEM16K reconstituted liposomes in the presence and absence of Ca^{2+}. Red dots and blue triangles represent data points derived from Sf9 and Expi293-expressed protein respectively, showing their equivalence.

Through this assay we determined that, similar to many other TMEM16 family scramblases, TMEM16K displays non-specific ion channel activity with, at least in this end point assay, minimal calcium dependence (**Fig. 7B**).

Chemical Matter

As part of our investigation into the scramblase activity of TMEM16K we found that the use of 50% shorter chain lipids such as DMPC and DMPG in proteoliposomes increased the scramblase activity of TMEM16K by a factor of 40. Indeed, for TMEM16K, the presence of short chain lipids has been shown to be a more potent activator of TMEM16K than calcium. Moreover, our higher resolution TMEM16K cryo-EM structure revealed the presence of a co-purified endogenous lipid, bound to a potential allosteric site between TM3-5, in the dimer interface cavity, behind the mobile TM3-5 unit that is key to opening and closing the channel. Longer chain lipids bound at this site could stabilise the closed conformation and/or shorter chain lipids bound at this site could allow the TM3-5 unit to rotate into the cavity, thus allowing the scramblase groove to open.

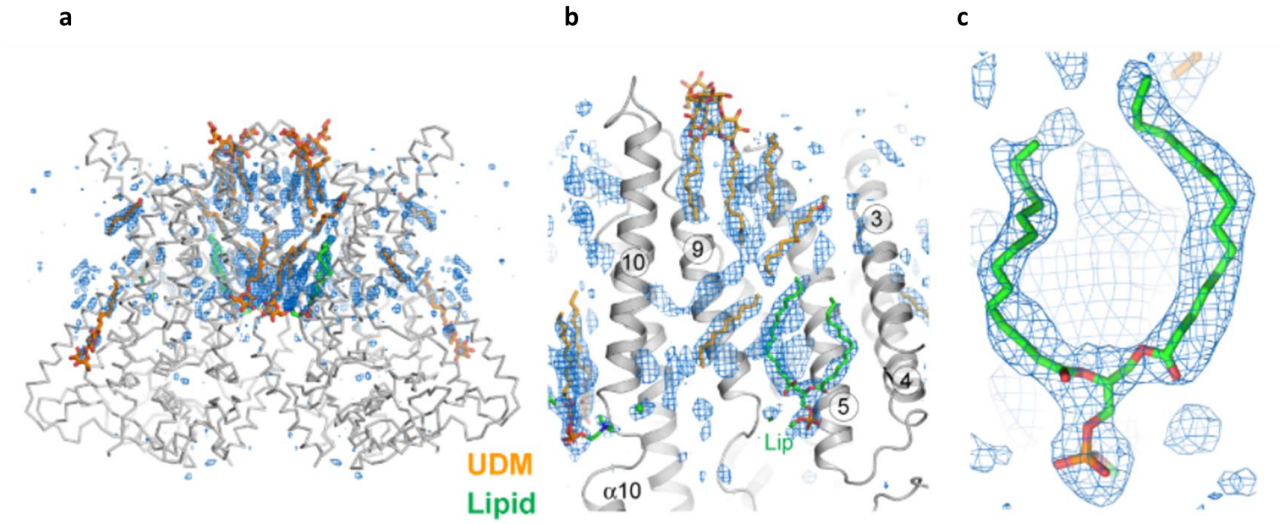

Fig. 8: (A) Density for bound Lipid (green) and Detergent (orange) Molecules in TMEM16K Structure. (B) Close up view of density for lipid and detergent molecules near the dimer interface between TMS 3,4,5,9 and 10^{B}. (C) Zoomed view of the unidentified bound lipid.

Other components

Working with Paolo Tammaro and John Christianson, we were able to show that TMEM16K is localised to the ER membrane when heterologously over-expressed in COS-7 cells and when expressed at native levels in U2OS cells. As part of this work we have characterised a polyclonal rabbit anti-TMEM16K antibody (Sigma, Cat ID: HPA051569). Native expression levels were too low to detect in HEK293T cells, but expression was clearly visible in immunocytochemistry with the U2OS cells, which are known to express TMEM16K at high levels. The antibody was shown to bind to purified TMEM16K in Westerns. It also detected a single band of the same size in HEK393T cells overexpressing TMEM16K, which was not present in untransfected HEK203T cells.

Collaborations

The localisation studies are a collaboration with Paolo Tammaro (Dept of Pharmacology, Oxford) and John Christianson (Nuffield Department of Rheumatology, Oxford). Initial functional studies to investigate ion channel activity involved Rebecca Sitsapesan (Dept of Pharmacology, Oxford) and Paolo Tammaro (Dept of Pharmacology, Oxford). The lipid scramblase and non-selective ion channel assays were performed by Maria Falzone and Alessio Accardi (Department of Physiology and Biophysics, Weill Cornell Medical School). We collaborate with Juha Huiskonen (OPIC and STRUBI, Oxford) for the cryo-EM structural work. We also work with Andrea Nemeth (Nuffield Department of Clinical Neurosciences, Oxford), a clinician working with patients with ataxias.

Future plans

- We plan to investigate the effects of disease mutations on TMEM16K activity.

- We will study the novel lipid binding site through mutagenesis and lipid replacement, to further characterise the role of short and long chain lipids in activation and/or inactivation of TMEM16K.
- We aim to develop higher throughput assays, so that we can screen compound libraries to identify lead compounds that modulate TMEM16K activity in cells.
- Once we have available effective and selective TMEM16K probe molecules, we aim to understand how loss of TMEM16K function changes lipid distribution in cells, leading to degeneration of the cerebellum.

CONCLUSION

Interest in the structure and function of TMEM16 proteins has emerged in parallel with increasing research in the role of TMEM16 proteins in human health. Mutation to TMEM16K causes autosomal recessive spinocerebellar ataxia Type 10 (SCAR10). SCAR10 diagnosis is difficult, but recent evidence suggest that the disease might represent one of the most common recessive spinocerebellar ataxias (13). Research into the role of TMEM16K in SCAR10 has hitherto been hampered by the logistical hurdles an intracellular membrane protein presents in terms of characterisation. The work we present in this TEP begins the process of deorphanising this rare disease; looking at its biochemical underpinnings with a view to set the scene for treatment.

We have identified TMEM16K as a phospholipid scramblase in the endoplasmic reticulum. Moreover, we have been able to over-express and purify TMEM16K for structural and functional characterisation. With purified protein we have produced an array of structures, using both X-ray crystallography and Cryo-EM, capturing both active and inactive conformations. The purified protein has also been used for functional assays measuring phospholipid scramblase activity, and non-specific ion channel flux. In combination, this work has suggested that TMEM16K can be regulated by lipid interactions, with both PLS activity and ion channel function augmented in the presence of the shorter chain lipids, which are much more prevalent in TMEM16K's ER environment. The presence of a bound lipid molecule in our high-resolution structure adds credence to this theory, as well as providing a potential means of therapeutic exploitation.

TEP IMPACT

The work behind the formation of the Target Enabling Package is currently under consideration for publication. A pre-publication print has been deposited at BioRxiv and can be viewed at:

- Bushell SR, Pike ACW, Falzone ME, et al (2018) The structural basis of lipid scrambling and inactivation in the endoplasmic reticulum scramblase TMEM16K. BioRxiv 447417.

FUNDING INFORMATION

The work performed at the SGC has been funded by a grant from Wellcome [106169/ZZ14/Z].

ADDITIONAL INFORMATION

Structure Files

PDB ID	Structure Details	Resolution (Å)
5OC9	Lipidic Cubic Phase Crystal Structure	3.2
6R65	Vapour Diffusion Crystal Structure	3.5
6R7X	CryoEM Structure in the presence of 2 mM Ca^{2+}	3.5
6R7Y	CryoEM Structure in the presence of 420 nM Ca^{2+}	4.2
6R7Z	Ca^{2+}-free TMEM16K structure (10mM EGTA)	5.1

Materials and Methods

Protein Expression and Purification

Cell Lines: DH10Bac, *Spodoptera frugiperda* (Sf9), Expi293F™ Cells (Thermo-Fisher, *Homo sapiens*)
Vector: pFB-LIC-Bse (Sf9 Expression), pHTBV1.1-LIC (Expi293 Expression)
Tags and Additions: C-terminal TEV cleavable 10His-FLAG Tag.

TMEM16K Construct Sequence:
MKVTLSALDTSESSFTPLVVIELAQDVKEETKEWLKNRIIAKKKDGGAQLLFRPLLNKYEQETLENQNLYLVGASKIRMLLGAE
AVGLVKECNDNTMRAFTYRTRQNFKGFDDNNDDFLTMAECQFIIKHELENLRAKDEKMIPGYPQAKLYPGKSLLRRLLTSGI
VIQVFPLHDSEALKKLEDTWYTRFALKYQPIDSIRGYFGETIALYFGFLEYFTFALIPMAVIGLPYYLFVWEDYDKYVIFASFNLIW
STVILELWKRGCANMTYRWGTLLMKRKFEEPRPGFHGVLGINSITGKEEPLYPSYKRQLRIYLVSLPFVCLCLYFSLYVMMIYF
DMEVWALGLHENSGSEWTSVLLYVPSIIYAIVIEIMNRLYRYAAEFLTSWENHRLESAYQNHLILKVLVFNFLNCFASLFYIAFV
LKDMKLLRQSLATLLITSQILNQIMESFLPYWLQRKHGVRVKRKVQALKADIDATLYEQVILEKEMGTYLGTFDDYLELFLQFG
YVSLFSCVYPLAAAFAVLNNFTEVNSDALKMCRVFKRPFSEPSANIGVWQLAFETMSVISVVTNCALIGMSPQVNAVFPESK
ADLILIVVAVEHALLALKFILAFAIPDKPRHIQMKLARLEFESLEALKQQQMKLVTENLKEEPMESGKEKATAENLYFQSHHHH
HHHHHHDYKDDDDK
(underlined sequence contains vector encoded TEV protease cleavage site, His and FLAG tag)

TMEM16K Construct Design and Cloning

The *Homo sapiens* TMEM16K gene, which encodes the TMEM16K/anoctamin-10 protein, was provided by the DNASU Plasmid collection. Coding DNA for the full length human TMEM16K sequence (NM_018075), Met1 to Thr660 (Uniprot ID: Q9NW15), was cloned into the baculovirus transfer vector pFB-CT10HF-LIC (available from The Addgene Nonprofit Plasmid Repository) for expression in *Spodoptera frugiperda* (Sf9) cells (Thermo-Fisher Scientific, Cat. No. 11496015). The vector adds a C-terminal TEV-cleavable His10-FLAG tag for purification. For mammalian expression, the same construct was also cloned into the pHTBV1.1-LIC baculovirus transfer vector (The BacMam vector backbone (pHTBV1.1), which was kindly provided by Professor Frederick Boyce, Massachusetts General Hospital, Cambridge, MA and adapted for ligation independent cloning in house) for expression in Expi239F cells (Thermo-Fisher Scientific, Cat. No. A14527). This vector also adds a TEV cleavable His10-FLAG tag to the C-terminus of the protein.

TMEM16K Expression

For both Sf9 and Expi293F Expression, baculoviral DNA, produced by transformation of DH10Bac with either the TMEM16K-pFB-CT10HF-LIC or TMEM16K-pHTBV1.1-LIC transfer vectors, were used to transfect Sf9 cells to produce baculovirus particles for transduction. Virus was amplified by transducing mid-log *Sf*9 cells ($2x10^6$ cells ml^{-1}) grown in Sf900II™ media with 2% fetal bovine serum. Cells were incubated on an orbital shaker for 65 hours at 27°C in 1 L shaker flasks. Baculovirus were harvested by centrifugation at 900 x *g* for 20 mins and the virus containing supernatant was used to infect 1 L of mid-log phase ($2x10^6$ cells ml^{-1}) cultures of Sf9 cells in Sf-900™ II Serum Free Medium (Gibco/Thermo-Fisher) in a 3 L flask, which were then grown for 72 hours at

27 °C on an orbital shaker. Cells were harvested by centrifugation at 900 x *g* for 15 mins, washed with Phosphate Buffered Saline (PBS), and pelleted again prior to flash freezing in liquid N_2, then stored at -80 °C until needed. For mammalian (Expi293F) expression, baculovirus were prepared in *Sf*9 cells as described for insect cell expression. 1L of Expi293F cell cultures (2 x 10^6 cells ml^{-1}) in Freestyle 293™ Expression Medium (Thermo-Fisher) were infected with high-titre P3 baculovirus (3% v/v) in the presence of 5mM sodium butyrate in a 2L roller bottle (Biofil). Cells were grown in a humidity controlled orbital shaker for 48 hours at 37 °C with 8% CO_2 before being harvested by the same process as for insect cells.

TMEM16K Cell Lysis and Solubilisation
Buffer A: 20 mM HEPES pH 7.5, 200 mM NaCl, 5 % glycerol v/v, 2 mM tris(2-carboxyethyl)phosphine (TCEP)

Sf9 or Expi293F cell pellets containing heterologously overexpressed protein destined for crystallographic analysis were resuspended in 30 ml / L equiv. original cell culture Buffer A and lysed by two passes through a Emulsiflex C5 homogeniser (Avestin). A 10:1 mixture of n-Undecyl-β-D-Maltopyranoside (UDM) / cholesteryl hemisuccinate (CHS) was added to the lysate, giving a final concentration of 1 % (w/v) for UDM and 0.1% for CHS, and incubated at 4 °C for 1 hour on a roller. Insoluble material was removed by centrifugation at 32,000 x g for 1 hour at 4 °C.

Immobilised Metal Affinity Chromatography and Gel Filtration Purification
Column 1: 50% slurry Talon™ Co^{2+}-Resin (1ml / L Original Cell Culture) in gravity column
Column 2: Superose 6 10/300 Size Exclusion Chromatography Column

The supernatant was supplemented with imidazole, pH 7.5 to a final concentration of 5 mM, and then a 50% slurry (v/v) pre-equilibrated Talon™ resin (1 mL of slurry per L original culture volume) was added. The suspension was then incubated at 4 °C on a roller for 1 hr. Talon resin was collected by centrifugation at 900 x g for 15 min and transferred to a gravity column where the remaining liquid was allowed to flow through. Subsequently, all buffer solutions were supplemented with 0.045%:0.0045% (w/v) UDM/CHS. The resin was washed with 25 column volumes of Buffer A with 20 mM imidazole, pH 7.5. TMEM16K was eluted with Buffer A + 250 mM imidazole. Peak elutions were then exchanged into Buffer A using Sephadex PD-10 desalting columns (GE Life Sciences). The C-terminal 10xHistidine-FLAG tag was removed by overnight incubation with 5:1 (w/w) TMEM16K: Tobacco Edge Virus (TEV) protease. TEV protease and contaminants were removed by adding 1.5 mL pre-equilibrated 50% Talon resin and batch binding at 4 °C for 1 hour on a rotator. The resin was removed by passing over a gravity column, with the resulting flow-through containing cleaved TMEM16K. Cleaved TMEM16K was concentrated to <1mL using a Vivaspin 20 centrifugal concentrator (GE Life Sciences) and further purified by size exclusion chromatography on a Superose 6 size exclusion column in Buffer A.

Structure Determination

Crystallisation
Purified TMEM16K was concentrated to 10-30 mg/ml using a Vivaspin 20 centrifugal concentrator with a 100 kDa molecular weight cut-off. Protein concentration was determined from the A280 using a Nanodrop spectrophotometer. TMEM16K was crystallised using both sitting drop vapour diffusion (VD) crystallisation and *in meso* in the lipidic cubic phase (LCP). VD crystals were grown in 0.1 M HEPES pH 7.0, 0.1 M calcium acetate, 22 % (v/v) PEG400, 0.05 mM C12E9 at a protein concentration of 10 mg/ml. For LCP crystallisation, 30 mg/ml TMEM16K was combined with 1-(7Z-hexadecenoyl)-rac-glycerol (monoacyl-glycerol 7.9, Avanti Lipids) in a 1:1.5 ratio to form a lipid cubic phase. A 50nl bolus of LCP-reconstituted TMEM16K was dispensed onto a glass LCP plate (Marienfeld, Germany) and overlaid with 800 nl of crystallisation solution. TMEM16K crystals grew in a LCP in a mother liquor containing 0.1 M MES pH 6.0, 0.1 M NaCl, 0.1 M $CaCl_2$, 30 % (v/v) PEG300. For both LCP and VD crystallisation, initial crystals appeared after 1 week and grew to full size within 3-4 weeks.

X-ray data collection and structure determination

All X-ray diffraction data were collected on the I24 microfocus beamline at the Diamond Light Source (Didcot, UK) from single crystals using a fine phi slicing strategy. Intensities were processed and integrated using XDS (14) and scaled using AIMLESS (15). The initial dataset collected on the LCP derived crystals was phased by molecular replacement using PHASER (16) with the nhTMEM16 structure (PDB: 4WIS) as an initial search model. Phase improvement was performed using *phenix.mr.rosetta* (17). The final model was built using COOT (18) and refined using BUSTER (19) using all data to 3.2 Å with appropriate NCS restraints. The final LCP model was subsequently used as a starting model for molecular replacement to solve the structure of detergent-solubilised TMEM16K using an anisotropic dataset collected from a crystal grown using sitting-drop vapour diffusion methods. The anisotropic nature of the VD dataset prevented it being solved using nhTMEM16 (the only high-resolution structure at the time) as a molecular replacement search model. Processing of the VD dataset was similar to that for the LCP crystals, with additional anisotropy correction performed using STARANISO (20). The model geometry of the VD dataset was improved by using LSSR target restraints to the LCP structure during BUSTER refinement in addition to TLS and NCS restraints.

The final LCP model encompasses residues Ser14 to Gln639. Several loops were poorly order and not modelled; residues 57-67 and part of the α7-α8 loop (residues 472-474) were disordered in chain A. The loops connecting either α5 and α6 or TM3-TM4 were poorly defined in both chains of the dimer and have also not been modelled. The final model also includes three Ca^{2+} ions per monomer along with an additional Ca^{2+} at the N-terminal end of TM10 on the dimer axis. The presence of Ca^{2+} ions at these sites was indicated by peaks in both anomalous difference and PHASER log-likelihood gradient (LLG) maps calculated using a 3.4 Å dataset with high multiplicity collected at a wavelength of 1.65 Å. Two Ca^{2+} ions in each dimer lie at the canonical two Ca^{2+} ion binding site and a third lies at the junction of TM10 and α10. All of these ions have bonds that are less than 2.5 Å to sidechains, suggesting the ions are not hydrated. The fourth Ca^{2+} ion identified in the anomalous difference maps lies on the dimer 2-fold axis, binding to the backbone of the ER loop between TM9 and 10. The greater than 4 Å interaction distances suggest that this ion is hydrated and is likely to be the result of the high (100 mM) [Ca^{2+}] used in the crystallisation conditions. This fourth ion is only present in the LCP dataset, not in the vapour diffusion structure, so the presence of this ion is not necessary for the open conformation to be formed. In addition, elongated density within the dimer interface were interpreted as MAG7.9 lipids.

Cryo-EM grid preparation

3 µl aliquots of TMEM16K protein purified in UDM/CHS, at a concentration of 5 mg/ml was either applied to grid directly (430nM Ca^{2+} samples) or supplemented with 2 mM $CaCl_2$ or 10 mM EGTA, then were applied to glow-discharged holey carbon grids (Quantifoil R 1.2/1.3 Cu 300 mesh). Grids were blotted at 80-100% humidity for 3-5 s at 5 °C and plunge-frozen in liquid ethane using a Vitrobot Mark IV, (FEI). Ca^{2+}-free TMEM16K grids were prepared in an identical manner using protein solution supplemented with 10 mM EGTA.

Cryo-EM structure determination methods

All initial processing was carried out in RELION 2.0 (21) & 3.0 (22). Frames in each movie stack were aligned and dose-weighted with MotionCor2 (23). CTF parameters were estimated using CTFFIND 4.0 (24). Dose weighted stacks were subjected to semi-automatic particle picking using Gautomatch. Particles were picked from a subset of micrographs and 2D classified to produce class averages. The resultant representative class averages were then used as templates in Gautomatch for autopicking the full image sets. Particles were subjected to multiple (5-6) rounds of reference-free 2D classification. An initial model was generated *ab initio* in RELION and used as a reference of 3D classification with no symmetry imposed. Particles belonging to the best / highest resolution class(es) were pooled and taken forward into a second round of 3D classification with C2 symmetry. Finally, particles from the highest resolution class were used for auto-refinement. The 2 mM and 500 nM datasets were further processed in RELION 3 (22) to take advantage of new particle polishing and CTF refinement routines. In both cases, two rounds of individual particle CTF refinement interspersed with a single step of Bayesian polishing and 3D auto-refinement produced the best maps. Further static 3D classification where no image alignment was performed with multiple (10) classes yielded a slightly better resolved reconstruction for the 2 mM $CaCl_2$ dataset. Local resolution estimation for each final reconstruction was performed with RELION (25). Post-processing was carried out in RELION using a mask extended by 12

pixels with an additional 12-pixel soft edge that excluded the detergent micelle surrounding the protein. Conformational homogeneity appears to be well maintained within each dataset and at no stage during 3D classification could we detect a subset of particles displaying a more open groove conformation. For the most part, TM3 and TM4 remain well resolved within and between different 3D classes indicating a lack of structural heterogeneity for the region that is responsible for defining the extent of the scramblase groove.

Model building was carried out manually using the 3.4 Å TMEM16K LCP crystal structure (PDB: 5OC9) as a template. Briefly, chain A of the crystal structure was roughly fitted into the 3.5 Å resolution 2 mM Ca^{2+} post-processed cryo-EM map in UCSF Chimera (26). Subsequent model building was carried out in COOT (18). The cytoplasmic domain was rotated into density and then appropriate sub-regions were fit to the density as rigid bodies. TM helices were fitted as rigid units or segmented where appropriate. The C-terminal α10 helix was rotated manually into position and side chains were fitted using preferred rotamers. The remodelled chain A was superposed onto chain B and globally fitted to the cryo-EM density to create the symmetric dimer. Refinement was carried out at 3.5 Å resolution against the post-processed RELION map (low pass filtered to 3.47 Å and sharpened with a *B*-factor of -112 $Å^2$) using *phenix.real_space_refine* (PHENIX v1.14) using NCS constraints, rotamerrestraints along with secondary structure restraints. Missing loop regions, not modelled in the crystal structure, were added and the calcium coordination was initially defined using *phenix.metal-coordination*. Subsequently the calcium coordination at both sites was maintained using distance restraints derived from the LCP X-ray structure. The final model encompasses all residues from Ser13-Lys641 and three Ca^{2+} ions per monomer. Some of the lipid / detergent like density around the TM domain at the dimer interface was modelled by six UDM molecules per monomer and a single phosphatidylcholine lipid. The precise identity of the lipid bound at the dimer interface between TM3, 5 and TM10 (of the adjacent monomer) is unknown.

The structure of the 430 nM Ca^{2+} complex is very similar to the 2 mM Ca^{2+} structure and only required minor adjustments to the poorly-resolved loop regions between α5-α6 and α7- α8. The density for the detergent and lipid molecules was present in the map but less convincing at this resolution and so these heterogroups were removed. The resultant model was refined against the 4.2Å RELION post-processed map (sharpened with a *B*-factor of -176$Å^2$) using *phenix.real_space_refine*. Model geometry was maintained using NCS constraints in combination with reference model restraints to the 2 mM Ca^{2+} structure.

The 2 mM Ca^{2+} structure also served as a template for the low resolution Ca^{2+}-free structure. The 2 mM Ca^{2+} model was initially docked into the map using Chimera and then refined using *phenix.real_space_refine* with global minimisation and morphing using default restraints/constraints and additional secondary structure restraints. A cryo-EM map, low-pass filtered to 5.1 Å resolution and sharpened with a *B*-factor of -150 $Å^2$, was used for all refinement and model building. The TM1-loop-TM2 region (residues 222-254) and the N-terminal end of TM10 required additional manual rebuilding/fitting in COOT. The cytoplasmic α7- α8 region was poorly resolved and truncated between residues 463-474. At this resolution, there was no obvious density for the amino acid sidechains and the vast majority were truncated to their C-beta atoms. Only the sidechains of prolines and a few large hydrophobic residues were retained. In addition, the Ca^{2+} ions were removed from the model. The resultant model was further refined with *phenix.real_space_refine* using NCS constraints, secondary structure restraints and reference model restraints to the 3.5 Å 2 mM Ca^{2+} structure. All structures / refinement protocols were validated by randomising the final models by applying coordinate shifts of up to 0.3 Å using the noise function in PDBSET (CCP4). The resultant shifted models were then refined against the corresponding post-processed half1 maps. Model-to-map Fourier shell correlations (FSCs) were then calculated with *phenix.mtriage* using either the final refined model against the full map (FSCsum) or the randomised half map1 refined model against either the half1 map (FSCwork) or the half2 map (FSCfree) not used in the validation refinement.

Functional Assays

Liposome reconstitution and lipid scrambling assay

Liposomes were prepared, as described previously (27), from a 7:3 mixture of 1-palmitoyl-2-oleoyl-glycero-3-phosphocholine (POPC) 1-palmitoyl-2-oleoyl-glycero-3-phosphoglycerol (POPG). Lipids in chloroform (Avanti),

including 0.4% w/w tail labelled NBD-PE, were dried under N2, washed with pentane and resuspended at 20 mg ml-1 in buffer B (150 mM KCl, 50 mM HEPES pH 7.4) with 35 mM 3-[(3-cholamidopropyl)dimethylammonio]-1-propanesulfonate (CHAPS). TMEM16K was added at 5 µg protein/mg lipids and detergent was removed using five changes of 150 mg mL^{-1} Bio-Beads SM-2 (Bio-Rad) with rotation at 4°C. Calcium or EGTA were introduced using sonicate, freeze, and thaw cycles. Liposomes were extruded through a 400 nm membrane and 20 µL were added to a final volume of 2 mL of buffer B supplemented with 0.5 or 2 mM $CaCl_2$ or 2 mM EGTA. The fluorescence intensity of the NBD (Excitation: 470 nm, Emission-530 nm) was monitored over time with mixing in a PTI spectrophotometer and after 100 seconds sodium dithionite was added at a final concentration of 40 mM. Data was collected using the FelixGX 4.1.0 software at a sampling rate of 3 Hz.

Bulk Flux Assay

Cl^- flux assay was conducted as described previously (28). Liposomes were prepared as per the lipid scramblase assay and equilibrated in external buffer with low KCl (1 mM KCl, 300 mM Na-glutamate, 50 mM HEPES, pH 7.4) by spinning through a Sephadex G50 column (Sigma-Aldrich) pre-equilibrated in external buffer. To complete the experiment, 0.2 mL of the flow through from the G50 column was added to1.8 ml of external solution and the total Cl^- content of the liposomes was measured using an Ag:AgCl electrode after disruption of the vesicle by addition of 40 µL of 1.5 M n-octyl-β-D- glucopyranoside (Anatrace). The fraction of liposomes containing at least one active TMEM16K ion channel, A, was quantified as follows:

$$A = 100 * (1 - \frac{\Delta Cl}{\Delta Cl_{PF}})$$

where ΔCl is the change in $[Cl^-]$ recorded upon detergent addition in protein-containing vesicles and ΔCl_{PF} is the Cl^- content of protein-free liposomes prepared in the same lipid composition on the same day.

References

1. Yang, Y. D., Cho, H., Koo, J. Y., Tak, M. H., Cho, Y., Shim, W. S., Park, S. P., Lee, J., Lee, B., Kim, B. M., Raouf, R., Shin, Y. K., and Oh, U. (2008) TMEM16A confers receptor-activated calcium-dependent chloride conductance. *Nature* **455**, 1210-1215
2. Brunner, J. D., Lim, N. K., Schenck, S., Duerst, A., and Dutzler, R. (2014) X-ray structure of a calcium-activated TMEM16 lipid scramblase. *Nature* **516**, 207-212
3. Suzuki, J., Umeda, M., Sims, P. J., and Nagata, S. (2010) Calcium-dependent phospholipid scrambling by TMEM16F. *Nature* **468**, 834-838
4. Marconi, C., Brunamonti Binello, P., Badiali, G., Caci, E., Cusano, R., Garibaldi, J., Pippucci, T., Merlini, A., Marchetti, C., Rhoden, K. J., Galietta, L. J., Lalatta, F., Balbi, P., and Seri, M. (2013) A novel missense mutation in ANO5/TMEM16E is causative for gnathodiaphyseal dyplasia in a large Italian pedigree. *Eur J Hum Genet* **21**, 613-619
5. Bolduc, V., Marlow, G., Boycott, K. M., Saleki, K., Inoue, H., Kroon, J., Itakura, M., Robitaille, Y., Parent, L., Baas, F., Mizuta, K., Kamata, N., Richard, I., Linssen, W. H., Mahjneh, I., de Visser, M., Bashir, R., and Brais, B. (2010) Recessive mutations in the putative calcium-activated chloride channel Anoctamin 5 cause proximal LGMD2L and distal MMD3 muscular dystrophies. *Am J Hum Genet* **86**, 213-221
6. Hicks, D., Sarkozy, A., Muelas, N., Koehler, K., Huebner, A., Hudson, G., Chinnery, P. F., Barresi, R., Eagle, M., Polvikoski, T., Bailey, G., Miller, J., Radunovic, A., Hughes, P. J., Roberts, R., Krause, S., Walter, M. C., Laval, S. H., Straub, V., Lochmuller, H., and Bushby, K. (2011) A founder mutation in Anoctamin 5 is a major cause of limb-girdle muscular dystrophy. *Brain* **134**, 171-182
7. Balreira, A., Boczonadi, V., Barca, E., Pyle, A., Bansagi, B., Appleton, M., Graham, C., Hargreaves, I. P., Rasic, V. M., Lochmüller, H., Griffin, H., Taylor, R. W., Naini, A., Chinnery, P. F., Hirano, M., Quinzii, C. M., and Horvath, R. (2014) ANO10 mutations cause ataxia and coenzyme Q_{10} deficiency. *Journal of Neurology* **261**, 2192-2198
8. Chamova, T., Florez, L., Guergueltcheva, V., Raycheva, M., Kaneva, R., Lochmuller, H., Kalaydjieva, L., and Tournev, I. (2012) ANO10 c.1150_1151del is a founder mutation causing autosomal recessive cerebellar ataxia in Roma/Gypsies. *J Neurol* **259**, 906-911

9. Vermeer, S., Hoischen, A., Meijer, R. P., Gilissen, C., Neveling, K., Wieskamp, N., de Brouwer, A., Koenig, M., Anheim, M., Assoum, M., Drouot, N., Todorovic, S., Milic-Rasic, V., Lochmuller, H., Stevanin, G., Goizet, C., David, A., Durr, A., Brice, A., Kremer, B., van de Warrenburg, B. P., Schijvenaars, M. M., Heister, A., Kwint, M., Arts, P., van der Wijst, J., Veltman, J., Kamsteeg, E. J., Scheffer, H., and Knoers, N. (2010) Targeted next-generation sequencing of a 12.5 Mb homozygous region reveals ANO10 mutations in patients with autosomal-recessive cerebellar ataxia. *Am J Hum Genet* **87**, 813-819
10. Bodranghien, F., Oulad Ben Taib, N., Van Maldergem, L., and Manto, M. (2017) A Postural Tremor Highly Responsive to Transcranial Cerebello-Cerebral DCS in ARCA3. *Frontiers in Neurology* **8**, 71
11. Hammer, C., Wanitchakool, P., Sirianant, L., Papiol, S., Monnheimer, M., Faria, D., Ousingsawat, J., Schramek, N., Schmitt, C., Margos, G., Michel, A., Kraiczy, P., Pawlita, M., Schreiber, R., Schulz, T. F., Fingerle, V., Tumani, H., Ehrenreich, H., and Kunzelmann, K. (2015) A Coding Variant of ANO10, Affecting Volume Regulation of Macrophages, Is Associated with Borrelia Seropositivity. *Mol Med* **21**, 26-37
12. Wanitchakool, P., Ousingsawat, J., Sirianant, L., Cabrita, I., Faria, D., Schreiber, R., and Kunzelmann, K. (2017) Cellular defects by deletion of ANO10 are due to deregulated local calcium signaling. *Cell Signal* **30**, 41-49
13. Nanetti, L., Sarto, E., Castaldo, A., Magri, S., Mongelli, A., Rossi Sebastiano, D., Canafoglia, L., Grisoli, M., Malaguti, C., Rivieri, F., D'Amico, M. C., Di Bella, D., Franceschetti, S., Mariotti, C., and Taroni, F. (2019) ANO10 mutational screening in recessive ataxia: genetic findings and refinement of the clinical phenotype. *Journal of Neurology* **266**, 378-385
14. Kabsch, W. (2010) XDS. *Acta Crystallographica. Section D, Biological Crystallography* **66**, 125-132
15. Evans, P. (2006) Scaling and assessment of data quality. *Acta Crystallographica. Section D, Biological Crystallography* **62**, 72-82
16. McCoy, A. J., Grosse-Kunstleve, R. W., Adams, P. D., Winn, M. D., Storoni, L. C., and Read, R. J. (2007) Phaser crystallographic software. *Journal of Applied Crystallography* **40**, 658-674
17. DiMaio, F., Echols, N., Headd, J. J., Terwilliger, T. C., Adams, P. D., and Baker, D. (2013) Improved low-resolution crystallographic refinement with Phenix and Rosetta. *Nature Methods* **10**, 1102-1104
18. Emsley, P., Lohkamp, B., Scott, W. G., and Cowtan, K. (2010) Features and development of Coot. *Acta Crystallographica. Section D, Biological Crystallography* **66**, 486-501
19. Bricogne, G., Blanc, E., Brandl, M., Flensburg, C., Keller, P., Paciorek, W., Roversi, P., Sharff, A., Smart, O., Vonrhein, C., and Womack, T. Buster v2.10.2 and 2.10.3. Global Phasing, Cambridge, UK
20. Vonrhein, C., Flensburg, C., Keller, P., Sharff, A., Smart, O., Paciorek, W., Womack, T., and Bricogne, G. (2011) Data processing and analysis with the autoPROC toolbox. *Acta Crystallographica. Section D, Biological Crystallography* **67**, 293-302
21. Kimanius, D., Forsberg, B. O., Scheres, S. H., and Lindahl, E. (2016) Accelerated cryo-EM structure determination with parallelisation using GPUs in RELION-2. *eLife* **5**
22. Zivanov, J., Nakane, T., Forsberg, B. O., Kimanius, D., Hagen, W. J., Lindahl, E., and Scheres, S. H. (2018) New tools for automated high-resolution cryo-EM structure determination in RELION-3. *eLife* **7**
23. Zheng, S. Q., Palovcak, E., Armache, J.-P., Verba, K. A., Cheng, Y., and Agard, D. A. (2017) MotionCor2: anisotropic correction of beam-induced motion for improved cryo-electron microscopy. *Nature Methods* **14**, 331-332
24. Rohou, A., and Grigorieff, N. (2015) CTFFIND4: Fast and accurate defocus estimation from electron micrographs. *Journal of Structural Biology* **192**, 216-221
25. Heymann, J. B. (2018) Guidelines for using Bsoft for high resolution reconstruction and validation of biomolecular structures from electron micrographs. *Protein Science: A Publication of the Protein Society* **27**, 159-171
26. Pettersen, E. F., Goddard, T. D., Huang, C. C., Couch, G. S., Greenblatt, D. M., Meng, E. C., and Ferrin, T. E. (2004) UCSF Chimera--a visualization system for exploratory research and analysis. *Journal of Computational Chemistry* **25**, 1605-1612

27. Malvezzi, M., Chalat, M., Janjusevic, R., Picollo, A., Terashima, H., Menon, A. K., and Accardi, A. (2013) Ca2+-dependent phospholipid scrambling by a reconstituted TMEM16 ion channel. *Nat Commun* **4**, 2367
28. Lee, B. C., Menon, A. K., and Accardi, A. (2016) The nhTMEM16 Scramblase Is Also a Nonselective Ion Channel. *Biophys J* **111**, 1919-1924

We respectfully request that this document is cited using the DOI value as given above if the content is used in your work.